Modelling the corrosion behaviour of Al_2CuMg coarse particles in copper-rich aluminium alloys

Christine Blanc, Alexandre Freulon, Marie-Christine Lafont, Yolande Kihn and Georges Mankowski

CIRIMAT, UMR CNRS 5085, ENSIACET, 118 route de Narbonne, 31077 Toulouse Cedex 04, France
CEMES, UPR 8011, 29 rue Jeanne Marvig, BP94347, 31055 Toulouse Cedex 04, France

Abstract

The corrosion behaviour of 2024 aluminium alloy in sulphate solutions was studied; attention was focused on the influence of coarse intermetallic Al_2CuMg particles on the corrosion resistance of the alloy. Model alloys representative of the aluminium matrix and of Al_2CuMg coarse intermetallics were synthesized by magnetron sputtering. Open-circuit potential measurements, current–potential curve plotting and galvanic coupling tests were performed in sulphate solutions with or without chlorides. Further explanations were deduced from the study of the passive films grown on model alloys in sulphate solutions. The results showed that model alloys are a powerful tool to study the corrosion behaviour of aluminium alloys.

Keywords: A. Aluminium; A. Intermetallics; A. Sputtered films; C. Passive films; C. Corrosion

1. Introduction
2.

There is significant interest in the corrosion behaviour of Cu-containing Al alloys, such as 2024 aluminium alloys (AA 2024), which remain of importance for aerospace applications. AA 2024 is a high-strength alloy in which a heterogeneous microstructure is developed by thermomechanical processing to obtain good mechanical properties. As a consequence, it is rather susceptible to localized corrosion, such as pitting corrosion, in many electrolytes. In a previous work [1], we studied the corrosion behaviour of 2024 aluminium alloys in chloride-containing sulphate solutions. The results showed that coarse intermetallic Al_2CuMg particles were preferential sites for pitting. When the alloy was polarized in sulphate solutions, these particles were homogeneously dissolved and, when chloride ions were added, pits formed preferentially on the intermetallics in certain experimental conditions, corresponding to the presence of a copper deposit on and around the intermetallics, due to the synergetic effect of sulphate and chloride ions towards copper. Other work, performed in nitrate solutions [2], confirmed that copper and magnesium-rich intermetallics strongly influenced the corrosion behaviour of AA2024. Their reactivity can be described by a three-step process consisting of homogeneous dissolution, copper redeposition followed by local dissolution of the surrounding matrix. Many other authors have discussed the importance of intermetallic particles as initiation sites for corrosion [3], [4], [5], [6], [7], [8], [9] and [10]. For example, Schmutz et al. [9] and [10] used atomic force microscopy (AFM), in situ AFM scratching and Volta potential mapping to study localized corrosion of Al alloys. The influence of copper-rich intermetallics on the corrosion resistance of aluminium alloys was clearly demonstrated by all these works but the mechanisms explaining the dissolution of the intermetallics, the copper enrichment and the pit nucleation at these sites are not so obvious even though many works have been performed on this topic [1], [3] and [11]. Zhu and Van Ooij [12] proposed a mechanism slightly different from that proposed by the authors of the present paper; they showed that the anodic Al_2CuMg particles dealloyed Al

and Mg during immersion in a neutral 0.6 M sodium chloride solution with the dealloying of Mg being the most severe. Simultaneously, strong dissolution of the Al matrix surrounding the coarse particles was also observed. This mechanism was similar to that proposed by other authors [3], [13] and [14]. For Buchheit et al. [3], selective dissolution of copper and magnesium-rich particles led to the formation of a highly porous copper-rich layer at the surface of the alloy. As a consequence, copper particles can be pulled from the surface and redistributed around the particles. It appears that significant work still is needed to really understand the corrosion behaviour of copper-rich aluminium alloys. To go further, many authors have used micrometer-scale electrochemical techniques [14] and [15]. But, electrochemical techniques used in the micrometer range are often expensive and difficult to use. To understand the corrosion behaviour of copper-rich aluminium alloys, another possibility is to study the electrochemical behaviour of model alloys representative of the different metallurgical phases present. Different means can be used to synthesize such model alloys (different melting techniques but also different physical deposition techniques). Thin films of Al–Cu alloys can be easily obtained using magnetron sputtering and are useful for such studies [16] and [17].

AA 2024 alloy is characterized by an Al matrix containing about 0.02 wt%Cu and two types of coarse intermetallic particles i.e., Al–38 wt%Cu–16 wt%Mg and Al–27 wt%Cu–7 wt%Mn–11 wt%Fe [2]. Including the fine strengthening particles, the mean Cu content of the matrix is about 4 wt%. The works previously mentioned showed the detrimental effect of Al_2CuMg coarse particles. Thus, in this study, attention was focused on the influence of copper and magnesium-rich particles on the corrosion behaviour of 2024 alloy. The electrochemical behaviour of the aluminium matrix containing the strengthening particles and of copper and magnesium-rich particles was studied; Al–4 wt%Cu and Al–55 wt%Cu–10 wt%Mg model alloys were deposited by magnetron sputtering. Open circuit potential (OCP) measurements were performed and polarization curves plotted in a sulphate solution with or without chlorides. Galvanic coupling tests were also performed in sulphate solutions. Taking into account that the nucleation step of pitting corrosion corresponds to passive film rupture and that galvanic coupling is probably due to local differences between the passive film grown on the Al matrix and that on the intermetallics, the passive films formed on the model alloys were studied in order to relate the electrochemical behaviour of the model alloys to the structure and chemical composition of the passive films grown on their surface. Thus, the alloys were polarized in sulphate solution and the oxide films grown on the surface were

observed by transmission electron microscopy (TEM) and analyzed by electron energy loss spectroscopy (EELS) and secondary ion mass spectrometry (SIMS).

2. Experimental

Material

Binary Al–4 wt% Cu alloy and ternary Al–55 wt%Cu–10 wt%Mg alloys were prepared by magnetron sputtering with separate high purity aluminium (99.999%), copper (99.99%) and magnesium (99.99%) targets. The substrates, onto which the alloys were deposited, consisted of mechanically polished (up to 1 μm diamond paste) 2017 aluminium alloy plates. The alloy layers were deposited at a rate of about 5 nm min^{-1} to reach a final thickness in the approximate range 150–250 nm determined from transmission electron microscopy (TEM) measurements. During the synthesis, the chamber was first evacuated to 2×10^{-7} mbar, with sputtering then carried out at 5×10^{-3} mbar in 99.998% argon. The results obtained for the model alloys were compared to those obtained on a 25 mm thick plate of 2024 T351 aluminium alloy. The T351 treatment consists in solution heat-treating at 500 °C, water quenching, straining, and tempering the alloy at room temperature for 4 days. Its composition was the following: Al base, Cu 4.54 wt%, Mg 1.51 wt%, Mn 0.63 wt%, Fe 0.17 wt%, Zn 0.08 wt%.

Electrochemical tests

The alloys deposited were potentiokinetically polarized in a 0.1 M sodium sulphate electrolyte (pH = 5.6). Other experiments were performed in a 0.1 M Na_2SO_4 + 0.004 M NaCl solution. A sample area of 2 cm^2 was exposed to a solution in contact with air, at room temperature. A three-electrode electrochemical cell was used including a platinum grid with a large surface area as the auxiliary electrode, the reference electrode being a saturated calomel electrode (SCE) with a Luggin capillary. All potentials quoted are with respect to the SCE reference. Solutions were prepared by dissolving the salts in distilled water. All chemicals used were analytical reagent grade. The samples were immersed in the solution (without further polishing except for 2024 alloy which was mechanically polished down to 4000 grit SiC

paper, ultrasonically cleaned in distilled water, and air dried) and the potential was immediately scanned at a rate of 15 mV min^{-1} from −1000 mV to 1000 mV/SCE. OCP measurements were also performed in a 0.1 M sodium sulphate solution, the samples being immersed in the electrolyte for 24 h. Further experiments consisted in performing some galvanic coupling tests in a 0.1 M sulphate solution by using the potentiostat in zero resistance ammeter (ZRA) mode with the auxiliary and reference connections of the potentiostat connected to a model alloy and the working connection of the potentiostat connected to another model alloy.

The chemical composition and the structure of the passive films grown on the model alloys were also studied. The model alloys were polarized at 1000 mV/SCE for 1 h in 0.1 M Na_2SO_4 solution to develop the passive films.

2.3. Microscopic observations and surface analysis

Suitable electron transparent sections of freshly deposited alloys and polarized alloys were examined by TEM using a Philips CM20T instrument with energy dispersive spectroscopy (EDS) and EELS facilities. Two methods were used to prepare the samples for TEM observations. In one method, the samples were sliced to a nominal thickness of about 30 nm by ultramicrotomy. In the second method, transparent sections were prepared from the thin films deposited on the substrates: samples were glued thin film to thin film, and embedded in resin in a tube. Then, the resulting sandwich was sliced into sections. The slices were ground down to about 100 μm thick and a dimple machined in the central region. Final electron transparency was obtained by ion milling on a precision ion polishing system (PIPS(tm), Gatan) using 5 kV Ar^+ ions. The composition of the alloys and of the passive films were determined by using EDS and EELS analysis. SIMS analyses were also performed on the polarized model alloys using a Cameca IMS4F in the profiling mode with an analyzed zone of 30 μm in diameter. Cs^+ ions were used for abrasion and the intensity profiles plotted from the recombination of Cs^+ ions with the analyzed chemical elements in order to reduce the matrix effect, i.e., to obtain intensity profiles closer to the concentration profiles.

3. Results and discussion

3.1. Structure and composition of the model alloys

Binary Al–Cu alloys and ternary Al–Cu–Mg model alloys were synthesized by magnetron sputtering to be representative respectively of the aluminium matrix and of the Al–Cu–Mg coarse intermetallic particles present in 2024 alloy. In such alloy, Al–Cu–Mg coarse intermetallic particles can correspond to S-phase (Al_2CuMg). We determined, in a previous work, a mean composition corresponding to 38 wt%Cu and 16 wt%Mg for Al–Cu–Mg coarse intermetallic particles present in 2024 alloy [2]. However, we also observed that the copper content of these intermetallics could vary over a wide range from 32 to 48 wt% for a just polished sample. Moreover, as said previously, these particles are very reactive and, in some conditions, a copper enrichment can occur leading to copper content on the particles of more than 80 wt%. Thus, the aim in the present work was to obtain a ternary model alloy with copper and magnesium contents corresponding to what could be the composition of copper and magnesium-rich intermetallics in 2024 alloy. Fig. 1 shows the TEM micrographs obtained on electron transparent sections respectively for Al–Cu model alloy (Fig. 1a) and for Al–Cu–Mg model alloys (Fig. 1b). Both model alloys consisted of thin films homogeneous in thickness; no defects such as cracks were observed so the electrolyte was in contact with the alloy layer and not with the substrate during the electrochemical tests. The alloy layers were about 300 and 500 nm thick for Al–Cu and Al–Cu–Mg model alloys respectively. TEM observations also showed that a polygranular structure was observed for Al–Cu model alloy with columnar grains crossing the whole alloy layer. The grains were about 60 nm wide and their length, measured perpendicularly to the substrate/alloy layer interface, corresponding to the model alloy thickness. For the Al–Cu–Mg model alloy, the morphology of the thin film was quite different with no grains observed suggesting an amorphous structure. The diffraction pattern obtained for both model alloys confirmed these observations (Fig. 2). For Al–4 wt%Cu alloy, the diffraction experiments showed a spotty ring pattern characteristic of a nano-crystallized structure (Fig. 2a). The medium grain size was less than 100 nm. The indexing of the diffraction pattern (Fig. 2b) was performed using the aluminium crystal cell parameters, which showed that the Al–Cu model alloy was a copper solid solution in aluminium (α-Al). It is well known that the solubility of copper in aluminium at room temperature is about 0.02 at%; in this work, EDS analysis was performed from the outer part of the alloy layer to the substrate/alloy layer interface. It showed that the Al–Cu model alloy was homogeneous in chemical composition. For this alloy representative of the matrix, the

chemical composition was Al–4 wt%Cu which corresponds to Al–2.8at%Cu. Thus, diffraction experiments showed that a solid solution was obtained even though a (α-Al + θ-Al_2Cu) 2-phase structure should have been observed according to the equilibrium phase diagram. This result was probably due to the experimental method used for the preparation of the material. We obtained the same results in another work [18]. For the Al–Cu–Mg model alloy, a continuous ring diffraction pattern was observed which showed that an amorphous structure was obtained for the alloy which was in agreement with TEM observations. EDS analysis showed that this model alloy was homogeneous relative to its chemical composition but the copper content was higher in comparison with the mean copper content determined by performing a statistical study on more than 20 Al–Cu–Mg particles present in 2024 alloy. However, the composition we determined, i.e., Al–55 wt%Cu–10 wt%Mg, corresponded to the chemical composition of some Al–Cu–Mg particles present in 2024 alloy since, as said previously, there is a significant dispersion in the chemical composition of this type of intermetallics. As a consequence, for the present study, we maintained sputtering conditions that led to the synthesis of the model alloys described above. Throughout the study, the matrix containing the strengthening phases was modeled with Al–4 wt%Cu thin film and the Al–Cu–Mg intermetallics by an Al–55 wt%Cu–10 wt%Mg model alloy. Concerning the amorphous structure of the latter model alloy, in other studies [18], we prepared binary Al–Cu alloys by magnetron sputtering and a nanocrystallized structure was obtained even with a copper content higher than 70 wt%. Thus, the amorphous structure we obtained for Al–Cu–Mg model alloy cannot be explained by the high proportions of alloying elements but might be due to the introduction of a third alloying element in significant proportions.

Fig. 1. TEM micrographs of (a) Al–4 wt.%Cu and (b) Al–55 wt.%Cu–10 wt.%Mg model alloys.

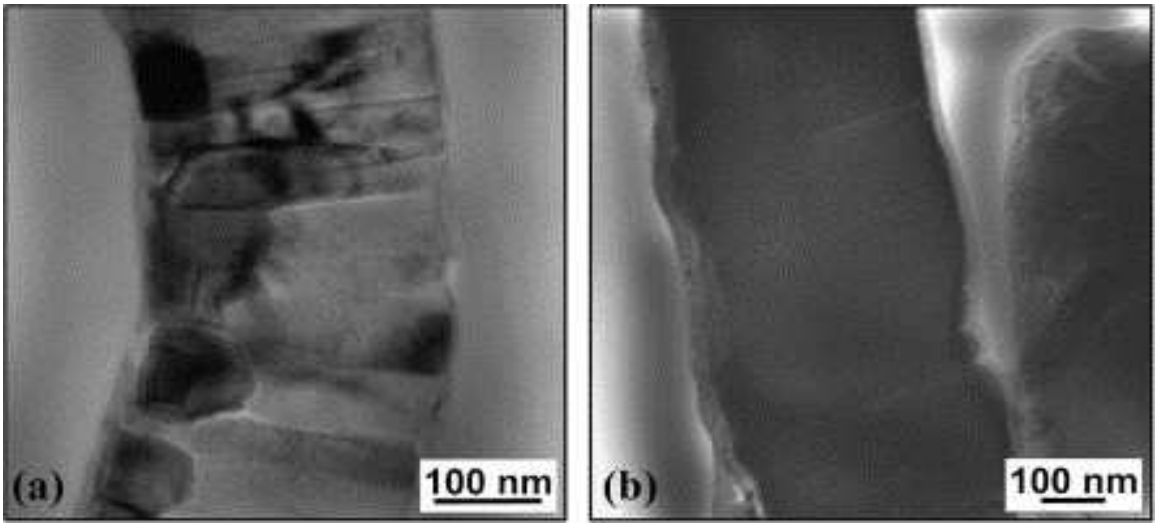

Fig. 2. Electron diffraction patterns of (a, b) Al–4 wt.%Cu and (c) Al–55 wt.%Cu–10 wt.%Mg model alloys.

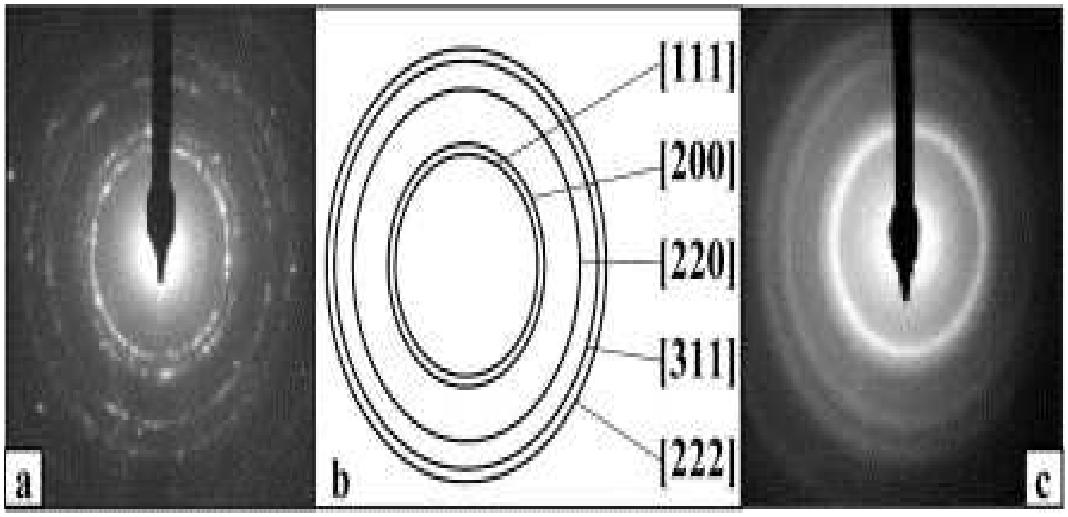

3.2. Electrochemical behaviour of Al–Cu and Al–Cu–Mg model alloys

Preliminary experiments were performed to compare the electrochemical behaviour of a pure aluminium thin film deposited on a 2017 Al alloy substrate and of a pure aluminium sheet (2 mm thick). OCP measurements and current–potential curves plotted in sulphate solutions showed that there were no differences in the electrochemical behaviour of these two samples. This confirmed that thin films synthesized by magnetron sputtering can be used to model a bulk material from an electrochemical point of view; it was thus assumed that comparison

between electrochemical tests performed on a bulk material (2024 alloy) and those obtained for the model alloys was relevant. Of course, the more similar the chemical composition and the crystallographic structure of the model alloy to that of the bulk material, the more representative the model alloy will be. Fig. 3 shows the OCP measured for Al–Cu and Al–Cu–Mg model alloys for 24 h in 0.1 M Na_2SO_4 solution. Results showed that, on immersion, the OCP strongly increased from cathodic to more anodic values (−400 mV/SCE) and then, after 24 h of immersion, stabilized at a potential of about −320 mV/SCE for Al–Cu alloy. For Al–Cu–Mg model alloy, OCP increased strongly on immersion to a more anodic value (about −150 mV/SCE) than that measured for Al–Cu model alloy and finally stabilized at about −200 mV/SCE after 24 h in sulphate solutions.

Fig. 3. Open circuit potential versus time in 0.1 M Na_2SO_4 solution for Al–4 wt.%Cu and Al–55 wt.%Cu–10 wt.%Mg model alloys.

Fig. 4 shows the potentiodynamic polarization curves plotted for both model alloys in a 0.1 M Na_2SO_4 solution. The potentiokinetic curve plotted for 2024 aluminium alloy is reported for comparison. For Al–Cu–Mg model alloy, the cathodic current density was about 5×10^{-4} A cm^{-2} close to that measured for 2024 alloy (about 10^{-4} A cm^{-2}). In contrast, the cathodic current density measured for Al–Cu alloy was much lower, about 5×10^{-6} A cm^{-2}. Thus, the corrosion behaviour of 2024 alloy was significantly influenced by the Al–Cu–Mg intermetallic particles in the cathodic range in spite of the fact that these coarse intermetallics only covered about 1% of the total surface area of the 2024 alloy. Al–Cu–Mg intermetallic particles promoted the cathodic reduction of oxygen, which explained the high cathodic current density measured for 2024 alloy. The cathodic current densities for the coarse intermetallics in 2024 alloy were high enough to determine the cathodic behaviour of 2024 alloy. The corrosion potential of 2024 alloy was similar to that measured for Al–Cu–Mg model alloy with E_{corr} being equal to −50 mV/SCE. This value corresponded to that obtained with the OCP measurements. This result differed from that obtained by Dimitrov et al. [19] who showed that the corrosion potential of an Al_2CuMg alloy sample was more negative than that of 2024 T3 Al alloy. In Dimitrov's work, the experiments were performed in a chloride solution which might explain the results since, as said previously, it can be assumed that the differences in the crystallographic structure observed between the Al–Cu–Mg alloy obtained by magnetron sputtering and the bulk one might not be the most significant parameter. By comparison with the corrosion potential measured for Al–Cu model alloy, the corrosion

potential of Al–Cu–Mg alloy was 150 mV shifted towards the more positive potentials. This result was in agreement with the OCP measurements (Fig. 3). In the anodic range, the electrochemical behaviour of 2024 alloy was similar to that of its matrix since the anodic current densities measured for 2024 alloys and Al–Cu alloy were similar and significantly lower than those measured for the Al–Cu–Mg model alloy. This result suggests that the passive films formed on the Al–Cu–Mg intermetallic particles were chemically different and less protective than those formed on the aluminium matrix. However, the influence of these particles on the anodic behaviour of 2024 alloy appeared much lower than in the cathodic range.

Fig. 4. Potentiodynamic polarization curves of AA2024, Al–4 wt.%Cu and Al–55 wt.%Cu–10 wt.%Mg model alloys in 0.1 M Na_2SO_4 solution. Potential scan rate: 15 mV min^{-1}.

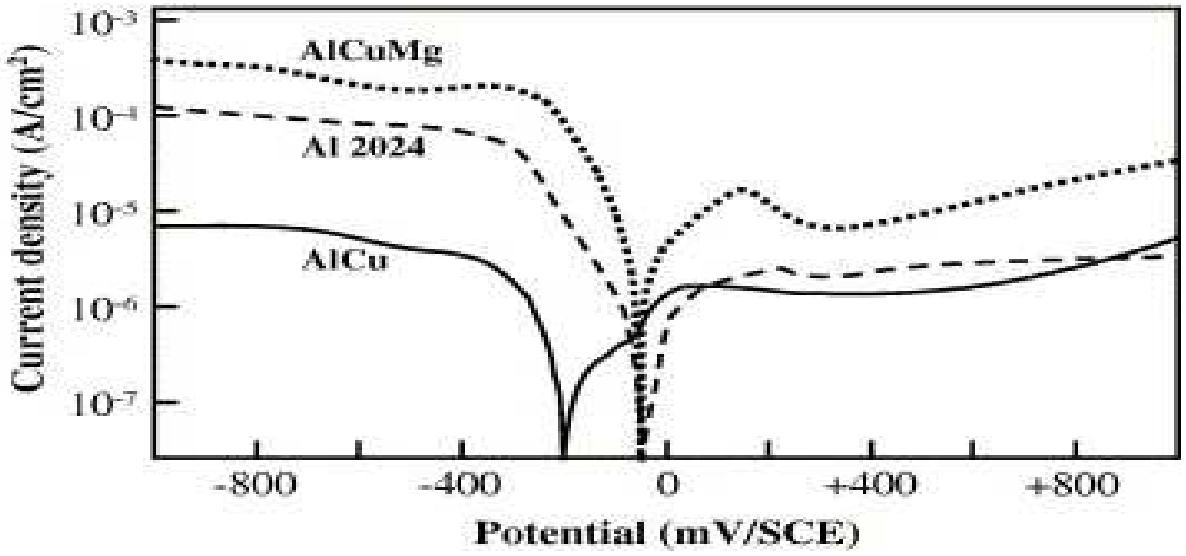

When chloride ions were present in the sulphate solutions (Fig. 5), significant differences were observed in the anodic range by comparison with the results obtained in sulphate solutions without chlorides. In the cathodic range, the electrochemical behaviour of Al–Cu–Mg alloy was again similar to that of 2024 alloy with cathodic current densities higher than those measured for the Al–Cu model alloy. But, in the anodic range, the electrochemical behaviour of 2024 alloy was now similar to that of the Al–Cu–Mg intermetallics and no longer to that of its matrix. In this potential range, we showed that, for the Al–Cu model alloy, representative of the matrix, there was a passivity plateau – this plateau was not very well-

defined with a passive current density between 5×10^{-5} and 10^{-4} A cm^{-2} – followed by a strong increase of the anodic current density corresponding to the formation of pits. The pitting potential was about −250 mV/SCE and was shifted about 250 mV towards more anodic potentials by comparison to those measured for the Al–Cu–Mg model alloy and for 2024 alloy. For these two last alloys, no passivity plateau was observed and the pitting potential was equal to the corrosion potential. This showed that the pitting susceptibility of 2024 alloy is related to the pitting behaviour of Al–Cu–Mg intermetallics, confirming the results obtained in previous works [1]. From Fig. 4, it could be assumed that the passive films formed on Al–Cu–Mg intermetallics was less protective than those formed on the aluminium matrix and Fig. 5 confirmed that, on addition of chloride, pits preferentially formed on the intermetallics.

Fig. 5. Potentiodynamic polarization curves of AA 2024, Al–4 wt.%Cu and Al–55 wt.%Cu–10 wt.%Mg model alloys in 0.1 M Na_2SO_4 + 0.004 M NaCl solution. Potential scan rate: 15 mV min^{-1}.

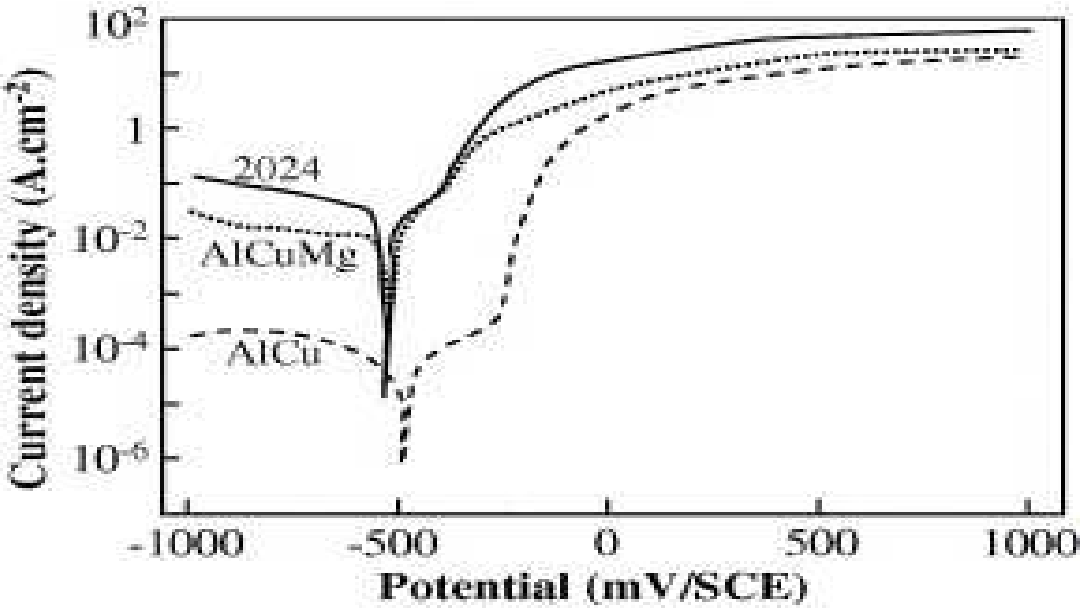

Further results were obtained with galvanic coupling tests between Al–Cu and Al–Cu–Mg alloys performed to reproduce the galvanic coupling that occurs in 2024 alloy. Fig. 6 shows that, at the beginning of the galvanic coupling test, Al–Cu–Mg dissolves while, after 2 min of immersion in the sulphate solution, it promotes the dissolution of the Al–Cu alloy. These

measurements corroborated the results given in the literature [2] and [20]. Brown and Kobayashi showed that the electrochemical behaviour of the Al–Cu–Mg particles varied from anodic to cathodic towards the aluminium matrix due to a variation of their chemical composition at the surface [20]. We observed the same phenomenon when we studied the electrochemical behaviour of 2024 alloy in nitrate solution [2]. It is therefore clear that the experiments performed on model alloys obtained by magnetron sputtering were very relevant to study the corrosion behaviour of commercial aluminium alloys.

Fig. 6. Current density versus time during galvanic coupling between Al–4 wt.%Cu and Al–55 wt.%Cu–10 wt.%Mg model alloys in 0.1 M Na_2SO_4 solution.

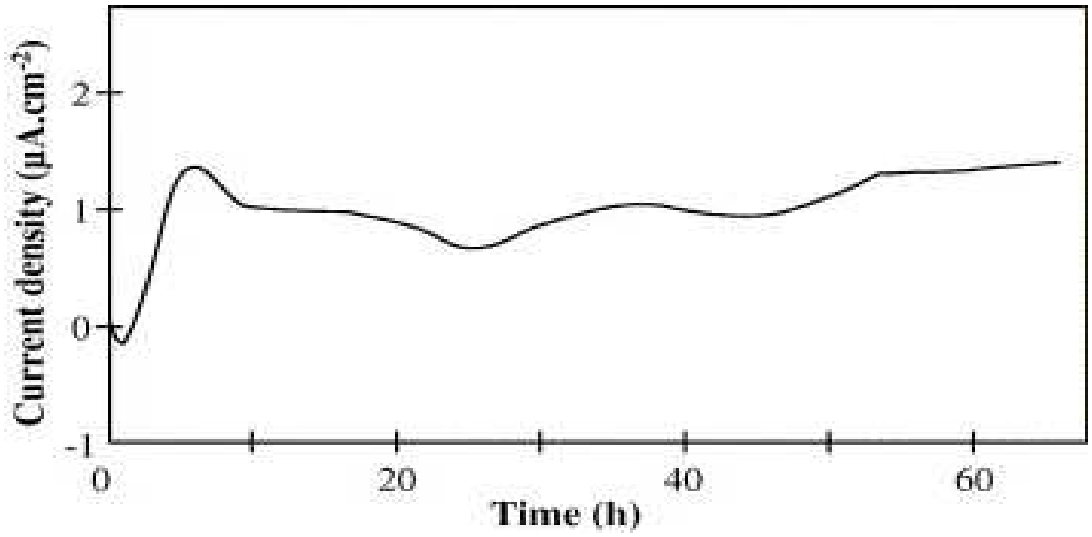

3.3. Study of the passive films grown on Al–Cu and Al–Cu–Mg model alloys

The results explained above confirm that Al–Cu–Mg intermetallics are preferential sites for pitting in 2024 aluminium alloy. Thus, to understand the corrosion behaviour of 2024 aluminium alloy, we studied the passive films formed on Al–Cu and Al–Cu–Mg model alloys in order to relate the electrochemical behaviour of the model alloys to the structure and chemical composition of the passive films on their surface and to understand the reactivity of Al–Cu–Mg intermetallics in 2024 alloy. In order to obtain passive films similar to those formed during the electrochemical tests (polarization curves for example), the model alloys were polarized in a 0.1 M sulphate solution and the potential was scanned from cathodic to anodic as for the current–potential curve plot. When a potential of 1000 mV/SCE was

reached, the sample was maintained at this final potential for 1 h. Fig. 7 shows the current density versus time plotted for both model alloys maintained at 1000 mV/SCE for 1 h in sulphate solution. For both model alloys, the current density remained constant for 1 h: it was lower for the Al–Cu model alloy than for the Al–Cu–Mg alloy which is in good agreement with the passive current density measured on the polarization curve (Fig. 4). The passivated samples were then observed by TEM. Fig. 8a shows TEM observations of the passive film grown on an Al–Cu model alloy polarized in 0.1 M Na_2SO_4 solution. The oxide film observed was about 20 nm thick and presented an amorphous structure as shown by the diffraction experiments. As the passive film observed was rather thin, several analytical techniques were used to confirm that this external layer observed by TEM unambiguously was a passive film. Both SIMS and X-ray photoelectron spectroscopy analysis performed on the Al–Cu model alloy before and after polarization in sulphate solution showed the presence of an oxide layer on the polarized alloy which was not detected before polarization. Further EELS analysis confirmed this observation. Fig. 9 shows the energy loss near edge structure (ELNES) part of EELS spectra of the Al K-edge obtained for Al–Cu alloy before and after polarization. Comparison with the ELNES spectra obtained for reference samples of metallic aluminium and of alumina showed that the aluminium was in a metallic state before polarization. After polarization, an alumina film was observed at the surface of the model alloy. The central zone of the thin film seemed to be composed of metallic aluminium and alumina while, near the 2017 substrate, aluminium was in a metallic state. EELS spectra at the Cu L_{23}-edge obtained for polarized Al–Cu model alloy showed that the alumina film was slightly enriched with copper. The copper content measured in the alumina film was much lower than that measured in the Al–Cu alloy. This observation was in good agreement with the results obtained by other authors who observed copper enrichment of oxide films formed on Al–Cu alloys. Habazaki et al. showed that the copper content in the anodic film formed on a bulk Al–4 wt%Cu alloy went on decreasing during the anodizing process due to the high diffusion rate of Cu^{2+} ions through the porous alumina film [21]. More recent studies showed that the anodizing of Al–Cu alloys proceeds in two stages [22]. In the initial stage, a copper-free alumina film is formed with copper accumulating near the alloy/oxide interface. In a following stage, when a sufficient concentration of copper has been achieved in the copper-enriched interface, the copper oxidizes and oxygen generation with the formation of bubbles in the alumina film is observed simultaneously. The authors thus showed that copper incorporation in aluminium had a detrimental effect on the anodic film growth.

Fig. 7. Passivity current density versus time for Al–4 wt.%Cu and Al–55 wt.%Cu–10 wt.%Mg model alloys in 0.1 M Na_2SO_4 solution.

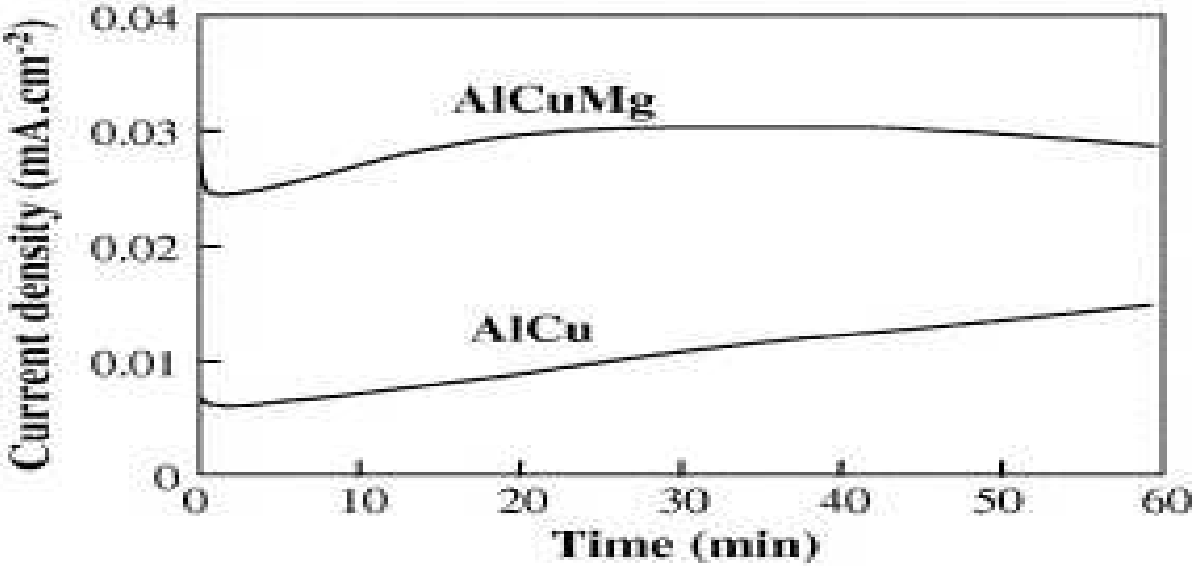

Fig. 8. TEM micrographs of (a and b) Al–4 wt.%Cu and (c) Al–55 wt.%Cu–10 wt.%Mg model alloys polarized for 1 h in 0.1 M Na_2SO_4 solution at 1 V/SCE.

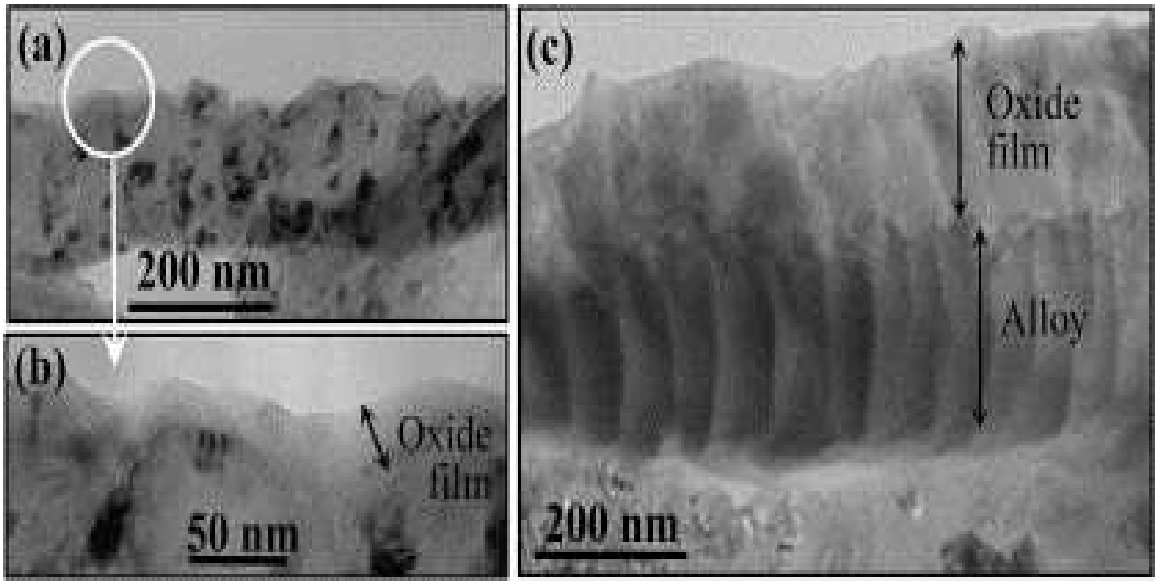

Fig. 9. Energy loss near edge structure (ELNES) part of electron energy loss spectroscopy (EELS) spectra of the Al-K-edge for Al–4 wt.%Cu model alloy (a) before and (b) after a 1 h polarization in 0.1 M Na_2SO_4 solution at 1 V/SCE.

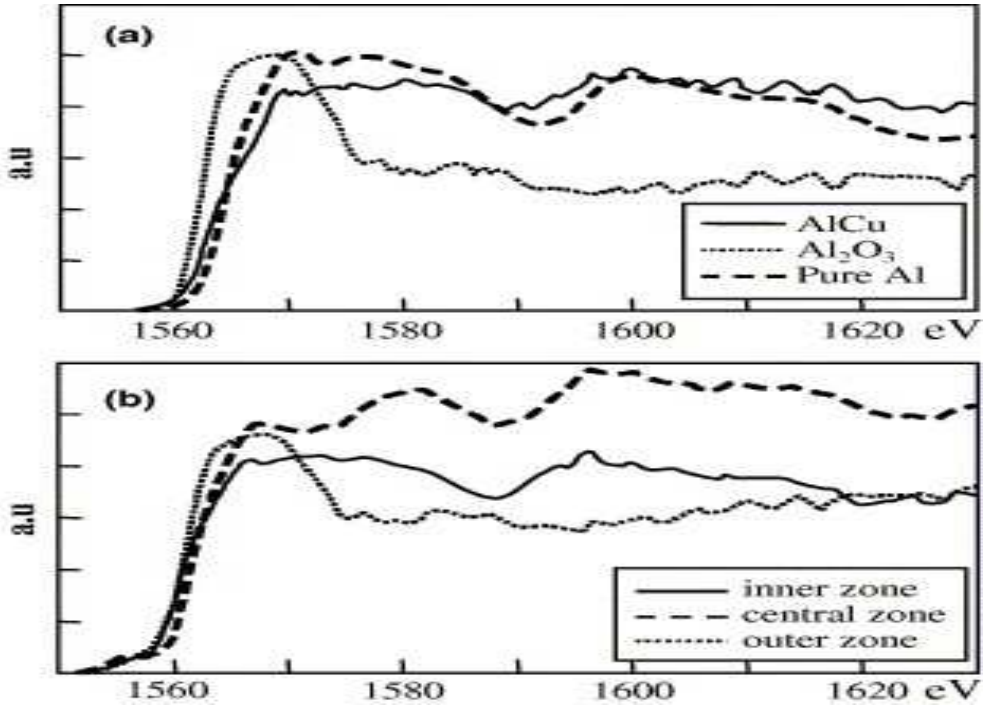

We also studied the ELNES profiles of the Cu L_{23}-edge. Fig. 10 shows that copper was present as metallic copper at the alloy/passive film interface and as oxidized copper in the film by comparison with ELNES profiles obtained for reference samples of metallic Cu and Cu oxides. The ELNES profiles also suggested that, in the outer part of the film, CuO was found while Cu_2O was detected in the inner part but it would be necessary to check this result by performing analysis on several polarized model alloys. Metallic copper present at the alloy layer/passive film interface might correspond to the copper-enriched layer described previously but this copper-enriched layer was not observed in the present work (except with these analyses) certainly due to the oxide film being so thin due to the low voltage applied during the polarization.

Fig. 10. Energy loss near edge structure (ELNES) part of electron energy loss spectroscopy (EELS) spectra of the CuL_{23}-edge for (a) reference samples and (b) Al–4 wt.%Cu model alloy after a 1 h polarization in 0.1 M Na_2SO_4 solution at 1 V/SCE.

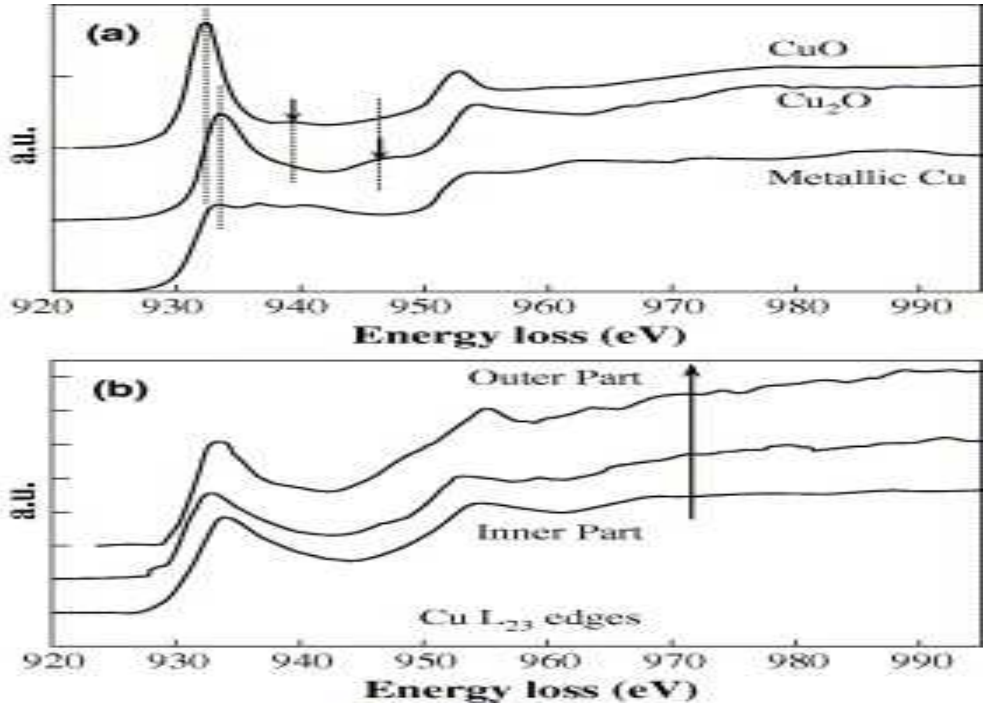

Fig. 8b shows TEM observations of the passive film formed on Al–Cu–Mg model alloys. For this alloy layer, the passive film was much thicker than that formed on Al–Cu alloy with a thickness of about 150–200 nm. This allowed the chemical composition of the passive film to be more easily studied. SIMS analyses were performed on the Al–Cu–Mg model alloy before and after polarization in sulphate solution. The samples were progressively sputtered to perform analysis from the outer part of the passive film to the inner part of the model alloy. Fig. 11 shows, for the polarized alloy, the profiles obtained for Al, Cu, Mg and O from recombination of these elements with Cs^+ ions to reduce the matrix effects. The profiles plotted for Al and O allowed the passive film/model alloy interface to be located. The Cu and Mg profiles showed that the passive film grown on Al–Cu–Mg alloy was enriched with copper, as for the Al–Cu model alloy, but also with magnesium. The copper content was nearly constant through the whole thickness of the passive film while the magnesium content was found to be much lower in the outer part of the film in comparison with the inner part of the film. This was explained by the high diffusion rate of magnesium through the alumina film [23]. EDS analysis confirmed these results showing that the magnesium content decreased from 7 wt.% in the central part of the passive film to 0.3 wt.% in the outer part. Thus, during the passivation of Al–Cu–Mg alloy, magnesium was rejected into the electrolyte. This could explain the electrochemical behaviour of Al–Cu–Mg alloy when immersed in sulphate solution: when Al–Cu–Mg alloy was coupled with Al–Cu alloy, at the beginning of

the experiment, Al–Cu–Mg dissolved. During the experiment, the passive film formed on Al–Cu–Mg alloy chemically evolved with magnesium going into the solution and the Al–Cu–Mg alloy then behaving as a cathode by comparison to the Al–Cu alloy.

Fig. 11. Secondary ion mass spectroscopy analysis of an Al–55 wt.%Cu–10 wt.%Mg model alloy after a 1 h polarization in 0.1 M Na_2SO_4 solution at 1 V/SCE.

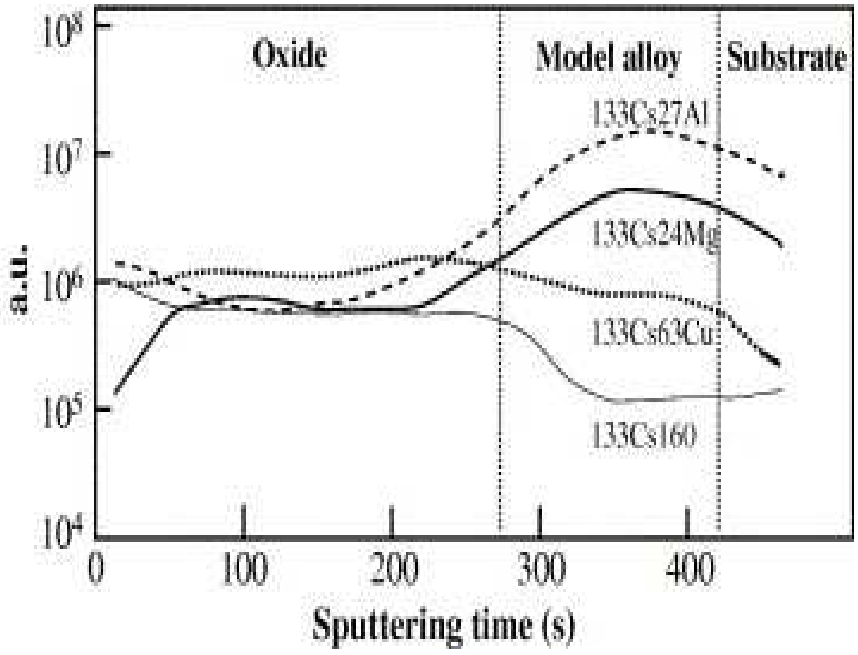

For both model alloys, passive films were observed but their thicknesses were very different. It could be suggested that the crystallographic structure (nanocrystallized or amorphous) of the alloy layer could significantly influence anodic film growth. However, it is well known that the oxide films on magnesium alloy are very thick [24]. Thus, it can be assumed that the incorporation of Mg in the passive film could explain this difference. Moreover, the results showed that the films formed on the model alloys representative of the aluminium matrix on one hand and of the Al–Cu–Mg intermetallics of 2024 alloy on the other hand were chemically different and that these chemical differences can explain the differences observed in the electrochemical behaviour of the two alloys. The presence of magnesium in the passive film grown on the Al–Cu–Mg model alloy might explain its less protective effect.

4. Conclusions

This work showed that model alloys synthesized by magnetron sputtering allowed relevant results to be obtained to study the corrosion behaviour of 2024 aluminium alloy. In sulphate solutions, the corrosion behaviour of 2024 alloy was significantly influenced by Al–Cu–Mg coarse particles in the cathodic range while, in the anodic range, its electrochemical behaviour was similar to that of its matrix. In the presence of chloride ions, the pitting susceptibility of 2024 alloy was related to Al–Cu–Mg coarse particles. The results showed that the differences in the electrochemical behaviour of the aluminium matrix and of the Al–Cu–Mg coarse particles present in 2024 aluminium alloy can be related to the chemical composition of the passive films grown on their surface.

References

C. Blanc, B. Lavelle and G. Mankowski, *Corros. Sci.* 39 (1997), p. 495.

C. Blanc, S. Gastaud and G. Mankowski, *J. Electrochem. Soc.* 150 (2003), p. B396.

R.G. Buchheit, R.P. Grant, P.F. Hlava, B. McKenzie and G.L. Zender, *J. Electrochem. Soc.* 144 (1997), p. 2621.

T.J. Warner, M.P. Shmidt, F. Sommer and D. Bellot, *Z. Metallkd.* 86 (1995), p. 494.

P. Campestrini, E. P.M. van Westing, H.W. van Rooijen and J.H.W. de Wit, *Corros. Sci.* 42 (2000), p. 1853.

T. Dimogerontakis, L. Kompotiatis and I. Kaplanoglou, *Corros. Sci.* 40 (1998), p. 1939.

V. Guillaumin and G. Mankowski, *Corros. Sci.* 41 (1998), p. 421.

J.D. Gorman, S.T. Johnson, P.N. Johnson, P.J.K. Paterson and A.E. Hughes, *Corros. Sci.* 38 (1996), p. 1977.

P. Schmutz and G.S. Frankel, *J. Electrochem. Soc.* 145 (1998), p. 2295.

V. Guillaumin, P. Schmutz, G.S. Frankel, in: A.C. Hillier, M. Seo, S.R. Taylor (Eds.), Localized In-Situ Methods for Investigating Electrochemical Interfaces, PV 99-28, The Electrochemical Society Proceedings Series, Pennington, NJ, 2000, p. 339.

R.G. Buccheit, M.A. Martinez and L.P. Montes, *J. Electrochem. Soc.* 147 (2000), p. 119.

D. Zhu and W.J. van Ooij, *Corros. Sci.* 45 (2003), p. 2163.

P. Schmutz and G.S. Frankel, *J. Electrochem. Soc.* 145 (1998), p. 2285.

Th. Suter and R.C. Alkire, *J. Electrochem. Soc.* 148 (2001), p. B36.

M. Shao, Y. Fu, R. Hu and C. Lin, *Mater. Sci. Eng. A* 344 (2003), p. 323.

Y. Liu, E.A. Sultan, E.V. Koroleva, P. Skeldon, G.E. Thompson, X. Zhou, K. Shimizu and H. Habazaki, *Corros. Sci.* 45 (2003), p. 789.

S. Garcia-Vergara, P. Skeldon, G.E. Thompson, P. Bailey, T.C.Q. Noakes, H. Habazaki and K. Shimizu, *Appl. Surf. Sci.* 205 (2003), p. 121.

J. Idrac, C. Blanc, G. Mankowski, M.-C. Lafont, G. Thompson, T. Hashimoto, P. Skeldon, Y. Liu, in: P. Schmuki (Ed.), Pits and Pores II: Formation, Properties and Significance for Advanced Materials, The Electrochemical Society Proceedings Series, in press.

N. Dimitrov, J.A. Mann, M. Vukmirovic and K. Sieradzki, *J. Electrochem. Soc.* 147 (2000), p. 3283.

G.M. Brown and K. Kobayashi, *J. Electrochem. Soc.* 148 (2001), p. B457.

H. Habazaki, M.A. Paez, K. Shimizu, P. Skeldon, G.E. Thompson, G.C. Wood and X. Zhou, *Corros. Sci.* 38 (1996), p. 1033.

S. Garcia-Vergara, F. Colin, P. Skeldon, G.E. Thompson, P. Bailey, T.C.Q. Noakes, H. Habazaki and K. Shimizu, *J. Electrochem. Soc.* 151 (2004), p. B16.

Y. Liu, P. Skeldon, G.E. Thompson and H. Habazaki, *Corros. Sci.* 44 (2002), p. 1133.

G. Baril, Ch. Blanc, M. Keddam and N. Pebere, *J. Electrochem. Soc.* 150 (2003), p. B488.

Corresponding author. Tel.: +33 5 62 88 57 08; fax: +33 5 62 88 56 63.

Original text : Elsevier.com